Contact mechanics and thermal conductance of carbon nanotube array interfaces

Baratunde A. Cola [*], Jun Xu [1], Timothy S. Fisher

School of Mechanical Engineering and Birck Nanotechnology Center, Purdue University, 1205 W. State Street, West Lafayette, IN 47907, USA

ARTICLE INFO

ABSTRACT

A model is developed in this work to predict the thermal contact resistance of carbon nanotube (CNT) array interfaces with CNT arrays synthesized directly on substrate surfaces. An analytical model for contact mechanics is first developed in conjunction with prior data from load–displacement experiments to predict the real contact area established in CNT array interfaces as a function of applied pressure. The contact mechanics model is utilized to develop a detailed thermal model that treats the multitude of individual CNT–substrate contacts as parallel resistors and considers the effects on phonon transport of the confined geometry that exist at such contacts. The influence of CNT array properties, *e.g.* diameter and density, are explicitly incorporated into the thermal model, which agrees well with experimental measurements of thermal resistances as a function of pressure for different types of interfaces. The model reveals that: (1) ballistic thermal resistance dominates at the CNT array interface; (2) the overall performance of CNT array interfaces is most strongly influenced by the thermal resistance at the contacts between free CNT ends and the opposing substrate surface (one-sided interface) or the opposing CNT array (two-sided interface); and (3) dense arrays with high mechanical compliance reduce the thermal contact resistance of CNT array interfaces by increasing the real contact area in the interface.

© 2009 Elsevier Ltd. All rights reserved.

1. Introduction

Carbon nanotubes (CNTs) are hollow tubular structures that can have single or multiple layers of ideally seamless graphene rolls. With lengths of several micrometers or more, these nanostructures can achieve aspect ratios as high as 10^4 [1]. Because of these unique structural features and strong carbon-to-carbon bonding, CNTs possess many exceptional vibrational, optical, mechanical, and thermal properties [1,2]. One of these attractive properties is an extremely high intrinsic thermal conductivity that is comparable to that of diamond [1–8]. Also, CNT arrays can exhibit high mechanical compliance and resilience [9–11]. Consequently, CNT arrays can be effective in reducing thermal interface resistance, potentially satisfying the increasing power dissipation challenge in microelectronics, and significant efforts have focused on using CNT and carbon nanofiber (CNF) arrays for this purpose [12–26]. While excellent performance of these materials has been observed experimentally, detailed modeling of heat flow through these arrays has not been reported, and the present work seeks to address this need by developing a combined thermo-mechanical model of CNT array thermal interfaces.

Low-to-moderate thermal interface resistance of CNT arrays has been measured by several techniques. Xu and Fisher [14] reported a resistance value of 20 mm² K/W at a contact pressure of 450 kPa for a Si-supported CNT array interfaced with Cu and tested with a reference bar method. Tong et al. [21] used an all-optical pump and probe phase sensitive transient thermo-reflectance method to measure a thermal resistance value of 12 mm² K/W for a Si–CNT–glass interface, which is very close to the result presented in [15]. Employing a photoacoustic technique, Amama et al. [22] and Cola et al. [23] measured thermal resistance values as low as 8 mm² K/W at a pressure 350 kPa for Si–CNT–Ag interfaces. Using the same photoacoustic technique, Cola et al. [20] measured thermal resistances near 4 mm² K/W at moderate pressures for an interface consisting of two CNT arrays in contact.

To complement experiments on CNT arrays used to reduce contact resistance, a thermal model is needed to explain and predict the resistance of CNT array interfaces with different properties for engineering applications and to optimize CNT array properties for improved performance. However, heat transfer through CNT array interfaces is very complicated. Using a variety of simplifying assumptions, Xu [27] developed an initial framework for describing heat transfer through CNT array interfaces. Neglecting the contributions of convection and radiation, the total thermal resistance of CNT array interfaces consists of three primary components [27]: (i) the resistances at interfaces of CNTs to their growth substrate, (ii) the resistances at interfaces of free CNT ends to the opposing substrate surface (one-sided interface) or the opposing CNT array

---

* Corresponding author. Present address: George W. Woodruff School of Mechanical Engineering, 801 Ferst Drive, Georgia Institute of Technology, Atlanta, GA 30332-0405, USA. Tel.: +1 404 385 8652; fax: +1 404 894 1658.
 E-mail address: baratunde.cola@me.gatech.edu (B.A. Cola).
[1] Present address: Honeywell Electronic Materials, 15128 E. Euclid Avenue, Spokane, WA 99216, USA.

Nomenclature

A nominal contact area (m²)
A_r real contact area (m²)
A_r' real contact area for two CNT arrays in contact (m²)
a radius (or size) of contact area (m)
$\bar{a}$ average radius (or size) of contact area (m)
b radius of cylinders (or CNTs) (m)
$\bar{b}$ average radius of cylinders (or CNTs) (m)
B effective bulk modulus of a CNT array (Pa)
c_1 adjustable parameter that captures variation in CNT array characteristics
c_2 parameter that determines the magnitude of saturation pressure
$C/$ volumetric lattice specific heat [J/(m³K)]
E_b bending modulus of an individual CNT (Pa)
E_r radial compressive modulus of an individual CNT (Pa)
F force (N)
h Planck's constant (6.626068 × 10⁻³⁴ m² kg/s)
Kn Knudsen number (l_{mfp}/a)
k thermal conductivity [W/mK]
k_B Boltzmann constant (1.38066 × 10⁻²³ J/K)
l_{mfp} phonon mean free path (m)
N number density of CNTs in contact with growth substrate (CNTs/mm²)
n number density of CNTs in contact with opposing substrate (CNTs/mm²)
n' number density of CNTs in contact with opposing CNT array (CNTs/mm²)
P nominal contact pressure (Pa)
P_f effective pressure on CNT array (Pa)
q'' heat flux (W/m²)
R thermal resistance (K/W)
R'' area-normalized thermal resistance (mm² K/W)
$\bar{R}''$ area-normalized thermal resistance based on average CNT radius (mm² K/W)
R_z average peak-to-valley height of surface profile (m)
T temperature (K)
t thickness (or length) (m)
t' incompressible thickness of CNT array (m)

t_o mathematically extrapolated CNT array thickness at zero pressure (m)
U lattice vibration energy with the Debye model (J/m³)
v_g frequency-independent phonon group velocity (m/s)

Greek symbols
Γ averaged phonon transmissivity
λ_d dominant phonon wave length (m)
σ_R CNT array's resistance to compression (Pa)
Φ volume ratio of carbon nanotubes in an array
Ψ constriction alleviation factor
υ Poisson's ratio

Subscripts
Ag silver
array CNT array
b ballistic resistance
c total resistance at individual CNT contacts
CNT carbon nanotube or CNT array
Cu copper
cd circular disc in half space
cs constriction
cy cylinder
eff effective
free ends opposing substrate or opposing CNT array interface
GS growth substrate
i arbitrary index corresponding to CNTs of different radius within an array
m mean or average
Ni nickel
OS opposing substrate
pl plane
root growth substrate interface
Ti titanium
vdW van der Waals contact
x contact width
y contact length

(two-sided interface), and (iii) the resistances within the CNT array itself (which can, in turn, include intra- and inter-CNT elements).

Molecular dynamics simulations and Boltzmann transport theory have been used for thermal modeling of solid–fluid interfaces [28,29] as well as solid–solid interfaces [30–34]. The sheer size and inherent variabilities of dense, vertically oriented CNT arrays make such approaches too expensive to use for CNT arrays; however, these approaches can provide useful sub-models to the overall interface model. In a temperature range of 10–100 K, Prasher [35] calculated the thermal boundary resistance between an individual multiwalled CNT and a Pt contact with CNTs vertically and horizontally oriented to the Pt surface using analytical approximations for phonon transport. In an equally low temperature range, Prasher et al. [36] calculated the thermal boundary resistance between an individual single-walled CNT and a Si substrate. The complementary challenge of estimating the total thermal resistance – and total contact area – achieved by the multitude of contacts that exists in a CNT array interface is addressed in the present work.

Before the application of a thermal model, the contact mechanics of an interface must be understood. Inspired by observations of CNT deformation at interfaces, a semi-empirical wool fiber compression theory [37,38], which was developed for the textile industry more than 60 years ago, is applied here to describe the deformation of substrate-supported CNT arrays under loading.

Employing classical contact mechanics principles and considering the effect of van der Waals forces at the nanoscale, we extend the theory to predict the contact area established in CNT array interfaces based on data from recent load–displacement experiments [39–41]. The CNT array contact mechanics model and detailed constriction and ballistic resistance analysis at individual CNT–substrate contacts are integrated in a thermal resistance model that describes heat transfer across CNT array interfaces. The model includes the effects of CNT array properties, *e.g.* diameter, density, and distribution, with the aim of providing useful information for optimizing CNT array thermal contact resistance.

2. CNT array contact mechanics model

2.1. CNT roots: contact at the growth substrate

Fig. 1 contains schematics of a vertically oriented CNT array directly synthesized on a flat substrate. Fig. 1a and c illustrate the section and plan views of CNT contacts to their growth substrate. To facilitate the thermal resistance analysis presented in later sections, the planar growth substrate is represented as a cluster of cylinders (sometimes called 'flux tubes') with radius $b_{GS,i}$ [42]. Centered on the axis of each cylinder at the surface is a protruding carbon nanotube with radius $b_{CNT,i}$. The sum of the substrate cylin-
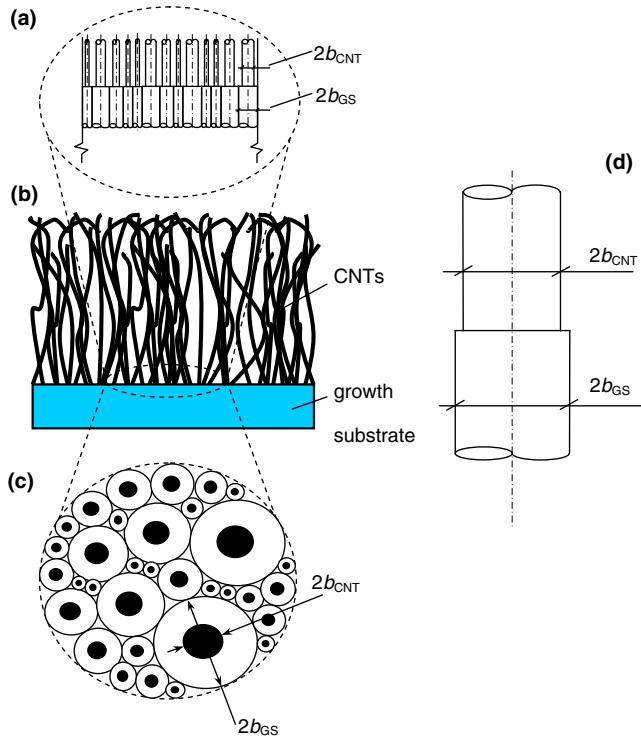
Fig. 1. Schematics (not to scale) of CNT array contacts to the growth substrate. (a) Cross-section view of CNT contacts to the growth substrate with a cylinder cluster approximation. (b) Vertically oriented CNT array synthesized on a flat substrate. (c) Plan view of CNT contacts to the growth substrate. (d) Constriction bounded by semi-infinite cylinders (flux tubes).

der cross-sectional areas is assumed to equal the nominal growth substrate surface area A. Fig. 1d shows the configuration of a single circular contact bounded by two semi-infinite cylinders (i.e., flux tubes [42]). This configuration is representative of the contact between the growth substrate and an individual CNT.

In an array, CNTs can have different radii $b_{CNT,i}$, and statistically, the number of $b_{CNT,i}$-sized CNTs per area is expressed here as $N_i(b_{CNT,i})$ (CNTs/mm^2). The size of the CNT contacts to the growth substrate are assumed to be equal to the radii of CNTs, $b_{CNT,i}$. The number density of spots with a contact size of $b_{CNT,i}$ at the growth substrate interface is the same as the number density of the $b_{CNT,i}$-sized CNTs, $N_i(b_{CNT,i})$, and the total number of contact spots per area on the growth substrate is

$$N = \sum_i N_i(b_{CNT,i}). \tag{1}$$

The growth substrate is assumed to be composed of cylinders with a statistical distribution of radii $b_{GS,i}$ (Fig. 1a and c) and corresponding number density $N_i(b_{CNT,i})$. Note that the sum of the cross-section areas of all the $b_{GS,i}$-sized cylinders equals the nominal substrate surface area (A), and

$$\sum_i N_i(b_{CNT,i}) \cdot b_{GS,i}^2 \cdot \pi = 1. \tag{2}$$

With a full macroscopic coverage of CNTs having a regular distribution over the substrate, we assume that the ratio $b_{CNT,i}/b_{GS,i}$ is uniform over the substrate for a given array. Based on CNT density and diameter distributions, the ratio of radii for the entire array can be determined as

$$\frac{b_{CNT}}{b_{GS}} = \sqrt{\frac{\sum_i N_i(b_{CNT,i}) \cdot b_{CNT,i}^2 \cdot \pi}{\sum_i N_i(b_{CNT,i}) \cdot b_{GS,i}^2 \cdot \pi}} = \sqrt{\sum_i N_i(b_{CNT,i}) \cdot b_{CNT,i}^2 \cdot \pi}. \tag{3}$$

The volume ratio of CNTs in an array can also be defined and estimated. The spatial volume of CNTs in an array can be estimated based on the CNT diameter range and density as

$$V_{CNT} = A \cdot \sum_i N_i(b_{CNT,i}) \cdot \pi \cdot b_{CNT,i}^2 \cdot t_{CNT,i}(b_{CNT,i}), \tag{4}$$

where $t_{CNT,i}(b_{CNT,i})$ is the characteristic length of CNTs with radius $b_{CNT,i}$. The array volume is the product of the nominal substrate surface area and mean array height t_m,

$$V_{array} = A \cdot t_m; \tag{5}$$

therefore, the volume ratio of CNTs in the array Φ is defined as

$$\Phi = \frac{V_{CNT}}{V_{array}} = \frac{\sum_i N_i(b_{CNT,i}) \cdot \pi \cdot b_{CNT,i}^2 \cdot t_{CNT,i}(b_{CNT,i})}{t_m}. \tag{6}$$

To simplify the estimation of this ratio, CNT lengths are assumed to be uniform for all radii, i.e. $t_{CNT,i}(b_{CNT,i}) = t_m$. Therefore, the CNT volume ratio is the same as the ratio of the total CNT cross-section area at the growth substrate ($A_{r.roots}$) to the nominal substrate surface area (A),

$$\Phi = \frac{V_{CNT}}{V_{array}} = \sum_i N_i(b_{CNT,i}) \cdot \pi \cdot b_{CNT,i}^2 = \left(\frac{b_{CNT,i}}{b_{GS,i}}\right)^2 = \frac{A_{r.roots}}{A}. \tag{7}$$

2.2. Free CNT ends: contact at opposing substrate or opposing CNT array

To evaluate the thermal resistance at the interfaces created by free CNT ends contacting an opposing substrate (one-sided interface) or opposing CNT array (two-sided interface), the deformation mechanics of CNT arrays must be ascertained first to define the geometry at the CNT contacts. Statistically, the number density of $b_{CNT,i}$-sized CNTs contacting an opposing substrate is $n_i(b_{CNT,i})$ (CNTs/mm^2), and for the two-sided, Velcro™-like structures considered later, the corresponding CNT number density is denoted by $n'_i(b_{CNT,i})$ (CNTs/mm^2). The total number density is defined as

$$n = \sum_i n_i(b_{CNT,i}) \left[\text{or } n' = \sum_i n'_i(b_{CNT,i})\right]. \tag{8}$$

Note that total number density n (or n'), in general, differs from the corresponding total number density N at the growth substrate, and n (or n') can never be greater than N. Currently, there is no clear method to determine the statistical distribution of $b_{CNT,i}$-sized CNTs that establish contacts of width $2a_{x,i}$ and length $a_{y,i}$ at the opposing substrate or opposing CNT array interface. Therefore, the total number density n, the average CNT radius defined as

$$\bar{b}_{CNT} = \frac{\sum_i b_{CNT,i} \cdot N_i(b_{CNT,i})}{\sum_i N_i(b_{CNT,i})}, \tag{9}$$

and the average contact geometry ($2\bar{a}_x$ and $\bar{a}_y$) defined below are used for estimating the total contact area at the interface to the free CNT ends.

2.2.1. Observations of CNT array deformation in interfaces

To investigate deformation mechanisms, CNT arrays were grown on Si and Cu substrates using microwave plasma chemical vapor deposition (MPCVD) [43] under previously reported process conditions with a trilayer catalyst configuration [14,20] (the thickness of the layer of catalyst metal, Fe, was adjusted to produce different CNT array characteristics). The Si-supported CNT arrays were interfaced to a flat Al plate under various loading conditions (Fig. 2a) and examined in the loaded condition using a scanning electron microscope (SEM). The average CNT diameter (20 nm) and the volume ratio of CNTs in the array (15%) were determined

from inspection of SEM images. Under moderate loading, the free ends of individual CNTs in the array were observed to bend at the Al surface while the portions of the CNTs near the growth surface remained primarily vertical (1st bending mode). This deformation creates an array of effective cylinder–plane contacts of width $2a_x$ between an individual CNT and the bulk solid surface (Fig. 2b). Upon sufficient increases in load, the CNTs collectively buckled at the interface. The illustrations and SEM images in Fig. 2a depict the CNT array deformation under various load conditions.

An interface consisting of a Si-supported CNT array mated to a Cu-supported CNT array (Fig. 2c) was also examined in the loaded condition using SEM. The average CNT diameter for both arrays was approximately 35 nm [20], and the volume ratio of CNTs for both arrays was approximately 20%. The SEM image in Fig. 2c shows that the free ends of individual CNTs bend at the interface of the two arrays creating cylinder–cylinder contact between touching CNTs (Fig. 2d). The illustrations in Fig. 2c depict the ex-

pected bending to buckling transition with increased load [9,41]. Notably, the free CNT ends of one array do not significantly penetrate into the mating array, presumably because of the relatively low bending strength of the individual, high-aspect-ratio ($>10^2$) CNTs and strong van der Waals forces between neighboring CNTs.

2.2.2. Analogy to wool fiber deformation

The mechanical compression of dense fibrous masses, such as CNT arrays, is a complex phenomenon yet one that occurs often in textile applications. van Wyk [37] demonstrated that compression of dense wool fibers can be interpreted in terms of a simple fiber bending model and derived a theoretical relation consistent with experimental observations. The theory predicts that the volume of a mass of loose wool fibers is inversely proportional to the cube root of the pressure exerted on the mass. The relation emerging from this proportionality depends on the bending strength of individual fibers, the volume ratio of fibers, and fiber-to-fiber mechanical interactions within the mass. Such fiber bend-
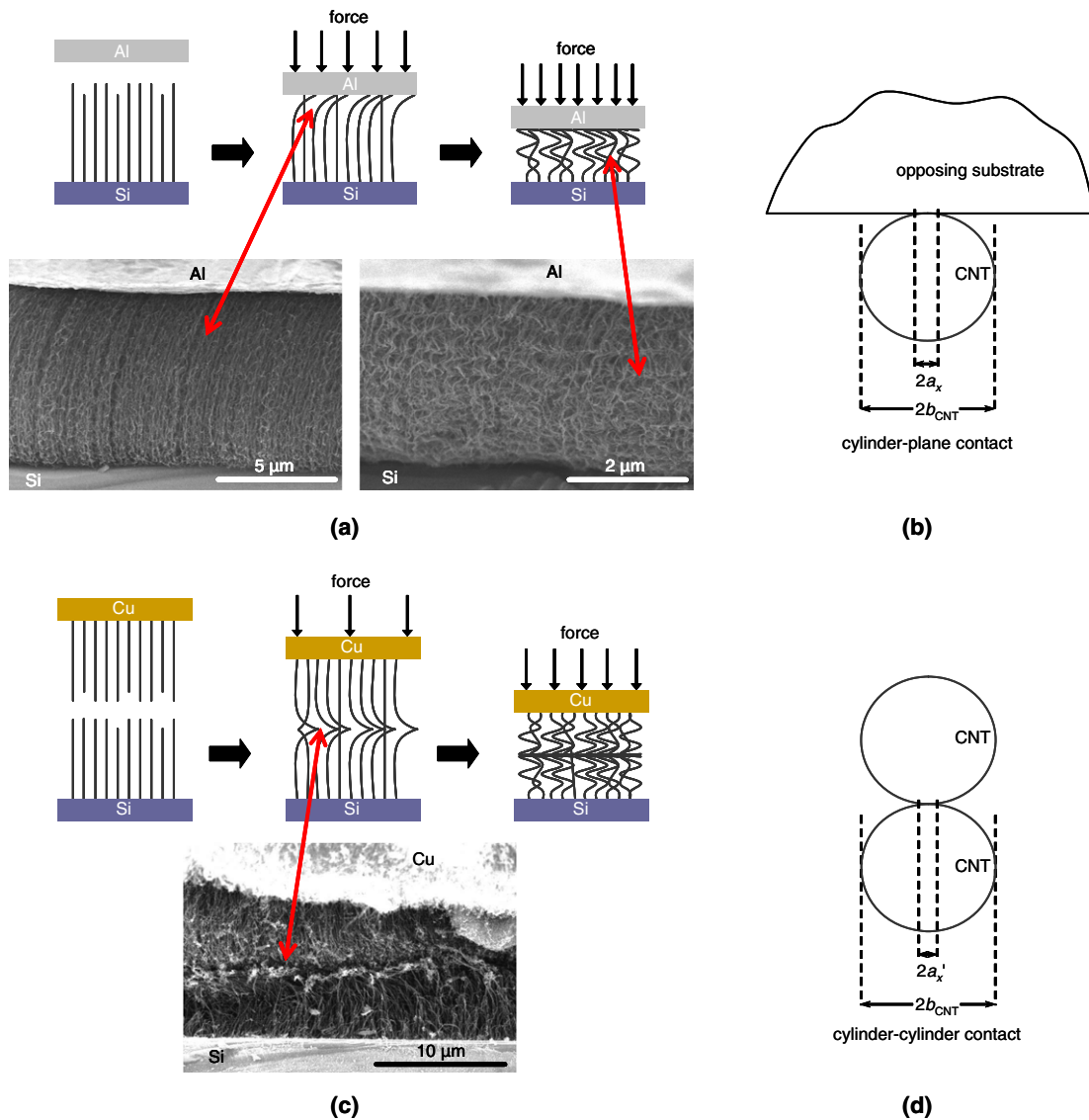
Fig. 2. Deformation and contact mechanisms in CNT array interfaces. (a) Illustrations and SEM images of a substrate-supported CNT array at various degrees of compression. The CNTs exhibit an average diameter of approximately 20 nm, and a volume ratio of approximately 15%. (b) Illustration of the cylinder–plane contact created at CNT-opposing substrate interfaces. (c) Illustrations and SEM image of two CNT arrays in contact, showing the bending of CNTs at the interface. The transition from CNT bending to buckling is displayed in the illustrations. The CNTs exhibit an average diameter of approximately 35 nm, and a volume ratio of approximately 20%. (d) Illustration of the cylinder–cylinder contact created at CNT–CNT interfaces.

ing is similar to our experimental observations of CNT bending (Fig. 2), and the principles of the derivation can be conceptually extended to represent the bending mechanism of CNT and CNF arrays. Indeed, recent force–displacement measurements on substrate-supported CNT arrays [39,41] and CNF arrays [40] exhibit a proportionality similar to wool compression, scaling as $t \propto P^{-1/3}$, where t is the height of the array under loading and P is the nominal applied pressure. Thus, van Wyk's relation corrected to consider the incompressible thickness of the fiber mass [38] may be applied to predict the thickness of substrate-supported CNT (and CNF) arrays under loading as

$$t = t' + (t_o - t') \cdot \left(\frac{P_f}{\sigma_R} + 1 \right)^{-1/3}, \qquad (10)$$

where t' is the incompressible thickness (*i.e.*, the thickness at which the structure becomes effectively incompressible [38]), t_o is the array thickness at zero applied pressure, P_f is an effective pressure – as opposed to the nominal contact pressure P – defined below, and σ_R is a parameter describing the array's resistance to compression.

The array thickness at zero pressure, t_o, is defined by Eq. (10) as the mathematically extrapolated array thickness intercept at zero applied pressure [37]. This thickness may slightly differ from the measured mean array thickness under no applied load, t_m [37]. We posit that small differences between t_m and t_o capture the interactions between the roughnesses of the mating surfaces and the variance in individual CNT heights within the array. van Wyk's derivation of Eq. (10) assumes that pressure is uniformly distributed on the surface of a wool mass with a volume ratio of fibers near unity, and treats compressed fibers as flat elements parallel to the plane of applied pressure [37]. Therefore, the pressure used in van Wyk's derivation requires modification when applying Eq. (10) to CNT arrays because volume ratios for CNT arrays are much lower and CNT elements, which have larger radii of curvature and radial stiffness, can not be approximated as flat in the plane of applied pressure. The effective pressure in Eq. (10) is thus defined as

$$P_f = \frac{P}{\left[\Phi \cdot \left(\frac{\bar{a}_x}{\bar{b}_{CNT}} \right) \right]}, \qquad (11)$$

where $\bar{a}_x$ is the average nanotube contact half width determined by considering van der Waals forces and elastic strain theory [44]. As illustrated in Fig. 3a, the van der Waals force (F_{vdW}) as a function of $\bar{b}_{CNT}$ has been calculated for different CNT contact scenarios in the limiting cases of dry air and water using the equations in Ref. [44], a Hamaker constant of 60×10^{-20} J for multiwalled CNT–metal contacts [45], and an equilibrium separation equal to the interlayer separation in graphite (0.335 nm). For dense CNT arrays under moderate pressure, van der Waals force at individual CNT–substrate or CNT–CNT contacts is at least an order of magnitude higher than the mechanical force applied at these contacts (these forces are compared below). Palaci et al. [46] measured a Young's modulus of multiwalled CNTs under radial compression of $E_r = 30 \pm 10$ GPa. This value is approximately equal to the Young's modulus of graphite along its c axis [47]. Therefore, $\bar{a}_x/\bar{b}_{CNT}$ is calculated using the elastic properties of graphite along its c axis ($E_r = 36$ GPa and $\upsilon = 0.012$) and the model described in Ref. [44]. Fig. 3b illustrates the variation of $\bar{a}_x/\bar{b}_{CNT}$ with $\bar{b}_{CNT}$.

A CNT array's resistance to compression is embodied by the parameter $\sigma_R = c_1 \cdot E_b \cdot \Phi^3$ in wool deformation theory, where E_b is the average bending modulus of an individual strand in the array that when applied to CNTs can range from 10 to 1000 GPa depending on the synthesis method and the level of CNT graphitization [48,49], and c_1 is an adjustable parameter that, in accordance with wool deformation theory [37], can account for variations in CNT array characteristics such as quality, average CNT aspect ratio, and
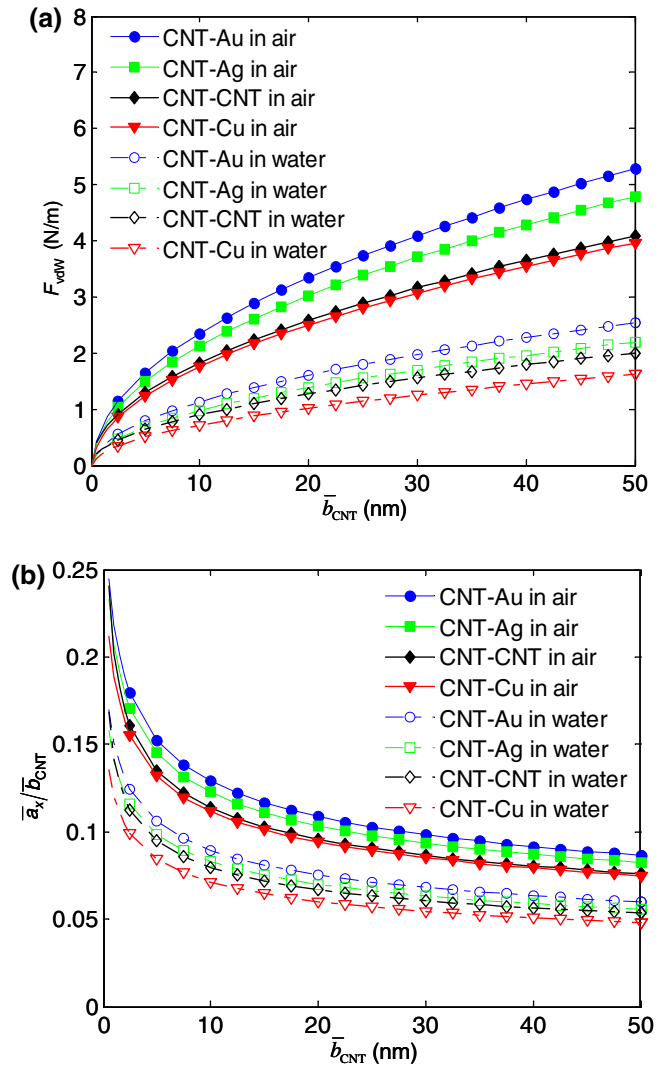

Fig. 3. van der Waals force F_{vdW} and normalized nanoscale contact width as functions of CNT radius $\bar{b}_{CNT}$. (a) Limiting cases of dry air and water for F_{vdW} at various CNT contact arrangements. The force is weaker in the presence of water. (b) Limiting cases for the normalized CNT contact width considering elastic, radial CNT deformation. Values near the middle of the limits are used for estimations in this study.

degree of CNT alignment in the array. As discussed below, the value of c_1 can be estimated from compressibility measurements.

Eq. (10) is semi-empirical, requiring experimental data to determine t', t_o, and c_1 (an E_b of 100 GPa [48] is assumed for the CNTs in this study). A least-squares method was used to fit Eq. (10) to data from previous experiments on the load–displacement characteristics of CNT array interfaces [39], and Fig. 4 illustrates the results. Eq. (10) can also be applied to the data of Zhang et al. [40] obtained from compression measurements on CNF arrays. Recent compression data obtained by Tong et al. [41] is difficult to fit with Eq. (10) because the range of strain in their study was much less than its full extent (*i.e.*, near the incompressible thickness).

The parameters estimated by fitting the compression data in Ref. [39] are given in Table 1; notably, the estimated value of initial thickness (t_o) closely matches the observed thickness (t_m) from SEM images, which we expect for relatively uniform CNT heights and small surface roughness. This agreement between an independently fitted parameter and an easily measured quantity lends support to the model's veracity. To reduce the number of unknowns involved in data fitting hereafter, we assume that $t_o = t_m$.
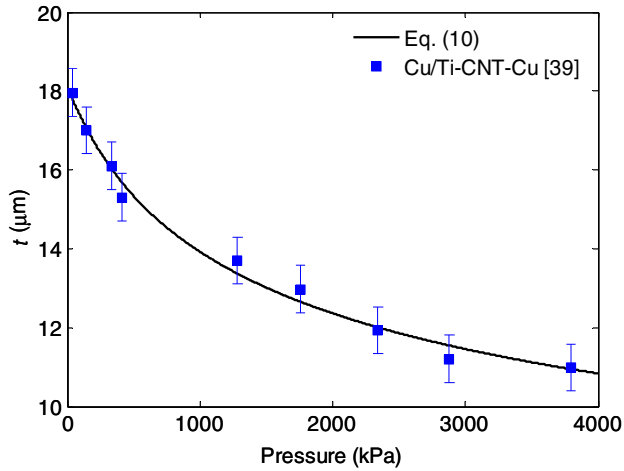
Fig. 4. Load–displacement data for a substrate-supported CNT array [39]. The solid line shows the model prediction (Eq. (10)) using the parameters listed in Table 1.

Table 1
Estimated compression parameters for the CNT array in Ref. [39].

Interface	Φ	$\bar{b}_{CNT}$ (nm)	t_m (μm)	t_o (μm)	t' (μm)	c_1	σ_R (MPa)
Cu/Ti–CNT–Cu [39]	0.25	25	18	18.12	3.65	0.018	28.73

A value of c_1 of approximately 0.018 was determined for the CNT array in Ref. [39]. For straight coarse wools, van Wyk estimated that c_1 should be of the order 10^{-2}; however, because c_1 includes variations in the characteristics of fibrous arrangements such as wool and CNT arrays, it can differ from sample to sample [37]. The close agreement between theory and experimental data, as shown in Fig. 4, suggests that compressibility measurements constitute a convenient method of predicting the effects of various properties and characteristics on the compliance of CNT arrays and therefore of predicting the real contact area at the free nanotube ends in CNT array interfaces as detailed in the following section.

2.2.3. Predicting real contact area

CNT array deformation is best described by elastic bending and reversible buckling [9,41]. Therefore, contact area can be related to the array's load–displacement response by elastic theory, where the free CNT ends bend at the opposing surface (or free CNT ends of an opposing array), thus creating contact along their side walls. As pressure increases, the total number density n and average length $\bar{a}_y$ of individual CNT contacts increases. Eq. (10), which captures collective CNT deformation within an array, can be used to derive an effective bulk modulus for CNT arrays as shown below. Using this effective bulk modulus, CNT arrays can then be modeled as thin films for application of Hertzian contact theory. Mikic [50] showed that at the same separation distance between contacting surfaces the contact area in elastic deformation is half the contact area in plastic deformation. This means that the effective bulk modulus is equal to approximately twice the hardness of the softer surface (the CNT arrays in this study). Utilizing this relationship between hardness and bulk modulus, as well as traditional contact theory [42], the ratio of real to nominal contact area between the free ends of a substrate-supported CNT array and an opposing solid can be estimated as

$$n \cdot \bar{a}_y \cdot 2\bar{a}_x = \frac{A_{r \cdot \text{free ends}}}{A} = \frac{2P}{B}, \tag{12}$$

where B, which is a function of P that is defined below, is the effective bulk or compressive modulus of the CNT array. By definition $n \leqslant N$, hence, the average contact length at the opposing substrate interface is given as

$$\bar{a}_y \geq \frac{A_{r \cdot \text{free ends}}}{2\bar{a}_x \cdot N \cdot A}. \tag{13}$$

Similarly, the contact area ratio between two opposing substrate-supported CNT arrays (i.e., two-sided CNT interfaces) can be estimated as

$$n' \cdot \bar{a}'_y \cdot 2\bar{a}'_x = \frac{A'_{r \cdot \text{free ends}}}{A} = \frac{4P}{B}, \tag{14}$$

where the extra factor of two is a consequence of the reduced effective modulus at the interface of equally soft materials [50]. Because $n' \leqslant N$, the average contact length at the interface of two CNT arrays in contact is given as

$$\bar{a}'_y \geq \frac{A'_{r \cdot \text{free ends}}}{2\bar{a}'_x \cdot N \cdot A}, \tag{15}$$

where N in this case is the CNT number density based on the average of both arrays.

The thermodynamic definition of bulk modulus can be expressed as $B = -t \cdot (dP/dt)$. Substituting Eq. (10) into this relation, the bulk modulus of CNT arrays under compression becomes

$$B(P_f) = \frac{3 \cdot (P_f + \sigma_R)}{\left[1 - \frac{t'}{t' + (t_o - t') \cdot \left(\frac{P_f}{\sigma_R} + 1 \right)^{-1/3}} \right]}. \tag{16}$$

Combining Eqs. (11), (12), and (16), the ratio of real to apparent contact area between a substrate-supported CNT array and a bulk solid becomes

$$\frac{A_{r \cdot \text{free ends}}}{A}(P_f) = \Phi \cdot \frac{\bar{a}_x}{\bar{b}_{CNT}} \cdot \frac{2P_f}{3 \cdot (P_f + \sigma_R)} \cdot \left[\frac{t_o - t'}{t' \cdot \left(\frac{P_f}{\sigma_R} + 1 \right)^{\frac{1}{3}} + t_o - t'} \right]. \tag{17}$$

As shown in several experiments [17,20,39,51], when $P_f > \sigma_R$ the real contact area in a CNT array interface is expected to approach a constant value – reaching a plateau at some point – under further increases in pressure. This condition is not explicitly satisfied by Eq. (17) because high-order P_f terms cause strong non-linear behavior as P_f becomes very large (i.e. $P_f \rightarrow \infty$). We address this issue by expanding the last term in Eq. (17), i.e., the bracketed expression, in a Taylor series of P_f about σ_R, and then neglecting the pressure terms of order two and higher as

$$\frac{A_{r \cdot \text{free ends}}}{A}(P_f) = \Phi \cdot \frac{\bar{a}_x}{\bar{b}_{CNT}} \cdot \frac{2P_f}{3 \cdot (P_f + \sigma_R)}$$
$$\cdot \left[\begin{array}{c} \frac{t_o - t'}{\sqrt[3]{2} \cdot t' + (t_o - t')} + \frac{t_o - t'}{\left[\sqrt[3]{2} \cdot t' + (t_o - t') \right]^2} \cdot \frac{t'}{3 \cdot \sqrt[3]{4}} + \\ \frac{t_o - t'}{\left[\sqrt[3]{16} \cdot t'^2 + 4 \cdot (t_o - t') \cdot t' + \sqrt[3]{4} \cdot (t_o - t')^2 \right]^2} \cdot \\ \left[\frac{2 \cdot \sqrt[3]{2}}{9} \cdot t'^3 + \frac{1}{3} \cdot (t_o - t') \cdot t'^2 + \frac{1}{9 \cdot \sqrt[3]{2}} \cdot (t_o - t')^2 \cdot t' \right] + \cdots \end{array} \right] \tag{18}$$

The first term in the bracketed expression of Eq. (18) is dominant. Therefore, in terms of the nominal contact pressure P (instead of P_f), the contact area ratio between the free ends of a substrate-supported CNT array and an opposing substrate can be expressed as

$$\frac{A_{r \cdot \text{free ends}}}{A}(P) = \frac{2}{3} \cdot \Phi \cdot \frac{\bar{a}_x}{\bar{b}_{CNT}} \cdot \frac{P}{\left(P + \sigma_R \cdot \Phi \cdot \frac{\bar{a}_x}{\bar{b}_{CNT}} \right)} \cdot \left[\frac{t_o - t'}{\left(\sqrt[3]{2} - 1 \right) \cdot t' + t_o} \right], \tag{19}$$

and the contact area ratio between two opposing substrate-supported CNT arrays is given as

$$\frac{A'_{r \cdot \text{free ends}}}{A}(P) = \frac{4}{3} \cdot \Phi \cdot \frac{\bar{a}'_x}{\bar{b}_{\text{CNT}}} \cdot \frac{P}{\left(P + \sigma_R \cdot \Phi \cdot \frac{\bar{a}'_x}{\bar{b}_{\text{CNT}}}\right)}$$
$$\cdot \left[\frac{(t_{o \cdot 1} + t_{o \cdot 2}) - t'}{\left(\sqrt[3]{2} - 1\right) \cdot t' + (t_{o \cdot 1} + t_{o \cdot 2})}\right]. \tag{20}$$

For two CNT arrays in contact, Φ and $\bar{a}'_x/\bar{b}_{\text{CNT}}$ are averages that include both arrays, and t' and σ_R are effective parameters that are characteristic of two interfacing arrays. We note that Eqs. (19) and (20) always produce values less than one (satisfying conservation of volume) because displaced CNT material that does not add to contact area is absorbed by an array, thereby increasing its density and stiffness. If the parameters t' and c_1 ($\sigma_R = c_1 \cdot E_b \cdot \Phi^3$) are known from compressibility measurements, then Eqs. (19) and (20) allow estimation of the real interfacial contact area as a function of applied pressure. Considering Eq. (19) and the data in Table 1, $A_{r \cdot \text{free ends}}/A$ for the CNT array interface in Ref. [39] is 2.6×10^{-3} at a moderate contact pressure of 100 kPa. At the same pressure, traditional contact theory [42] predicts A_r/A assuming plastic deformation for soft metals such as Al and In to be 6.0×10^{-4} and 5.0×10^{-3}, respectively.

The pressure-dependent contact area achieved in CNT array interfaces (i.e., the contact area established at the free CNT ends interface) is principally governed by the parameters Φ and σ_R (the expression $(t_o - t')/\left[(\sqrt[3]{2} - 1) \cdot t' + t_o\right]$ is later shown to assume values between 0.5 and 1). The CNT contact area increases with increasing Φ (volume ratio of CNTs in the array) and with decreasing σ_R (the array's resistance to compression); therefore, an optimal condition of CNT array properties that maximize contact area exists (because $\sigma_R = c_1 \cdot E_b \cdot \Phi^3$). Moreover, engineering CNT array interfaces such that the total array deformation, $t_m - t'$, is greater than the average peak-to-valley height of asperities R_z on the surface in contact with the free CNT ends can facilitate increased interface contact by minimizing adverse effects of surface roughness [18], which are not explicitly accounted for in the present theory.

The pressure at individual CNT contacts due to applied interface pressure (i.e., mechanical pressure) can be estimated as $P \cdot A_{r \cdot \text{free ends}}/A$. For example, at a large applied pressure of $P = 10^4$ kPa, the mechanical pressures at the individual, dry nanotube contacts in the CNT array interface of Ref. [39] are of the order of 10^5 kPa, which is an order of magnitude less than the van der Waals pressures at these contacts. Consequently, computing $\bar{a}_x/\bar{b}_{\text{CNT}}$ considering van der Waals forces alone is a reasonable assumption for dense CNT array interfaces at moderate pressures.

3. Thermal model

3.1. Constriction resistance at CNT–growth substrate interfaces

Because of the vertical contact that exists at CNT roots (see Fig. 1), the diffusive thermal constriction resistance from an individual CNT to its growth substrate can be modeled as constrictions bounded by semi-infinite cylinders (see Fig. 1d) [42]. Considering the contact mechanics at the CNT–growth substrate interface described above, the constriction resistance at the contact between an individual CNT with radii $b_{\text{CNT},i}$ and the growth substrate is defined as

$$R_{cs \cdot \text{GS}-\text{CNT},i} = R_{cd,i}(b_{\text{CNT},i}, k_{\text{GS}}) \cdot \Psi_i(b_{\text{CNT},i}, b_{\text{GS},i}), \tag{21}$$

where k_{GS} is the thermal conductivity of the growth substrate. $R_{cd,i}$ is the well known constriction resistance of a circular disk in half space [42], expressed as

$$R_{cd,i}(b_{\text{CNT},i}, k_{\text{GS}}) = \frac{1}{(4k_{\text{GS}} \cdot b_{\text{CNT},i})}, \tag{22}$$

and Ψ_i is the constriction alleviation factor [42]. In general, a smaller $b_{\text{CNT},i}/b_{\text{GS},i}$ ratio produces larger Ψ_i, and when $b_{\text{CNT},i}/b_{\text{GS},i}$ is near unity, Ψ_i approaches zero. A simple power relation introduced by Bahrami et al. [52] is adopted here to represent Ψ_i as

$$\Psi_i(b_{\text{CNT},i}, b_{\text{GS},i}) = \left(1 - \frac{b_{\text{CNT},i}}{b_{\text{GS},i}}\right)^{1.5}. \tag{23}$$

The area-normalized constriction resistance at each CNT growth site becomes

$$R''_{cs \cdot \text{GS}-\text{CNT},i} = \frac{\pi \cdot b_{\text{CNT},i} \cdot \Psi_i(b_{\text{CNT},i}, b_{\text{GS},i})}{4k_{\text{GS}}}. \tag{24}$$

In the present model CNTs are treated as solid cylinders for the constriction resistance estimates. Yovanovich and Schneider [53] showed for wall thicknesses ranging from 10% to 90% of the flux tube outer radius b, circular annular contact constriction resistance decreases from 1.24 to 1.08 times R_{cd}. Therefore, the solid cylinder approximation is reasonable for the multiwalled CNTs here, which have typical wall thicknesses that are greater than 50% of the outer tube radius [14].

According to its definition, Ψ_i in Eq. (23) is never larger than unity. Therefore, it can be approximated as unity to estimate the upper limit of constriction resistance. At room temperature, and with a CNT radius range of 2–50 nm, the upper limit of $R''_{cs \cdot \text{Ti}-\text{CNT},i}$ (Ti coated growth surface – $k_{\text{Ti}} = 21.9$ W/m K [54]) is 1.8×10^{-3} mm^2 K/W. A Ti surface was chosen for the foregoing analysis because it is commonly employed to facilitate the direct synthesis of well adhered CNT arrays [14,19,20,22–24].

3.2. Constriction resistance at interfaces to free CNT ends

3.2.1. Contacting an opposing substrate

The free ends of CNTs in an array bend under loading at the opposing substrate interface creating contact similar to a cylinder lying on a plane (see Fig. 2a and b). The analytical solution for diffusive thermal constriction resistance in this configuration is provided in [55]. Considering a statistical distribution of $b_{\text{CNT},i}$-sized CNTs and the CNT array contact mechanics detailed above, the thermal constriction resistance at the surface of an individual CNT is given as

$$R_{cy,i}(a_{x,i}, a_{y,i}, b_{\text{CNT},i}, k_{\text{CNT}}) = \frac{1}{a_{y,i} \pi k_{\text{CNT}}} \ln\left(\frac{4b_{\text{CNT},i}}{a_{x,i}}\right) - \frac{1}{2a_{y,i} k_{\text{CNT}}}. \tag{25}$$

Similarly, constriction resistance in the opposing substrate near the contact of width $2a_x$ is given as

$$R_{pl,i}(a_{x,i}, a_{y,i}, b_{\text{CNT},i}, k_{\text{OS}}) = \frac{1}{a_{y,i} \pi k_{\text{OS}}} \ln\left(\frac{2b_{\text{CNT},i}}{\pi a_{x,i}}\right). \tag{26}$$

The total constriction resistance at the cylinder–plane CNT contact is

$$R_{cs \cdot \text{CNT}-\text{OS},i} = R_{cy,i}(a_{x,i}, a_{y,i}, b_{\text{CNT},i}, k_{\text{CNT}}) + R_{pl,i}(a_{x,i}, a_{y,i}, b_{\text{CNT},i}, k_{\text{OS}}), \tag{27}$$

and the area-normalized resistance can be formulated as

$$R''_{cs \cdot \text{CNT}-\text{OS},i} = \frac{2a_{x,i}}{\pi k_{\text{CNT}}} \ln\left(\frac{4b_{\text{CNT},i}}{a_{x,i}}\right) - \frac{a_{x,i}}{k_{\text{CNT}}} + \frac{2a_{x,i}}{\pi k_{\text{OS}}} \ln\left(\frac{2b_{\text{CNT},i}}{\pi a_{x,i}}\right). \tag{28}$$

Assuming the radius of CNTs to have an upper limit of 50 nm, the contact half width $a_{x,i}$ can be conservatively estimated as 5 nm (see Fig. 3b). With $k_{\text{CNT}} = 3000$ W/m K at room temperature [8], conservative estimates of the room-temperature $R''_{cs \cdot \text{CNT}-\text{OS},i}$ for opposing substrates of Cu ($k_{\text{Cu}} = 401$ W/m K [54]), Ni ($k_{\text{Ni}} = 90.7$ W/m K [54]), and Ag ($k_{\text{Ag}} = 429$ W/m K [54]) are $R''_{cs \cdot \text{CNT}-\text{Cu},i} =$

1.7×10^{-5} mm^{2}K/W, $R''_{cs \cdot CNT-Ni,i} = 6.7 \times 10^{-5}$ mm^{2}K/W, and $R''_{cs \cdot CNT-Ag,i} = 1.6 \times 10^{-5}$ mm^{2}K/W , respectively. The Cu, Ni, and Ag opposing surfaces were selected based on CNT array interfaces reported in recent experiments [14,17,20,22–24].

3.2.2. Interface of opposing CNT arrays

At the interface of two contacting CNT arrays, individual CNTs in each array bend under loading to create cylinder–cylinder contacts as illustrated previously in Fig. 2c and d. Therefore, the diffusive constriction resistance at individual contact locations between two CNTs with equal radii $b_{CNT,i}$ is quantified using Eq. (25) as

$$R_{cs \cdot CNT-CNT,i} = 2 \cdot R_{cy,i}\left(a'_{x,i}, a'_{y,i}, b_{CNT,i}, k_{CNT}\right), \qquad (29)$$

and the area-normalized constriction resistance for this case is

$$R''_{cs \cdot CNT-CNT,i} = \frac{4a'_{x,i}}{\pi k_{CNT}} \ln\left(\frac{4b_{CNT,i}}{a'_{x,i}}\right) - \frac{2a'_{x,i}}{k_{CNT}}. \qquad (30)$$

Using the conservative values of $b_{CNT,i} = 50$ nm and $a'_{x,i} = 5$ nm, $R''_{cs \cdot CNT-CNT,i}$ is estimated to be 4.5×10^{-6} mm^2 K/W at room temperature.

3.3. Size effects on phonon transport

As discussed earlier, individual CNT contacts should possess a characteristic dimension less than or equal to the CNT radius b_{CNT}, which typically ranges from 2 to 50 nm for multiwalled tubes. For such small contacts, size effects play a significant role in contact resistance when the Knudsen number Kn (for this analysis, the ratio of phonon mean free path l_{mfp} to the contact size a) is near unity or larger [31]. Heat transfer in CNTs is phonon-dominated with a typical value of $l_{mfp} \approx 500$ nm at room temperature [8], and more generally the phonon mean free path for most crystalline solids is ~100 nm. The dominant energy carriers at all CNT contacts are phonons, including CNT–metal contacts [35]. Therefore, Kn at CNT contacts can be much greater than unity, such that the probability of the phonon's passing through the contact area is very low and the phonon-mediated transport is ballistic [56].

3.3.1. Ballistic thermal resistance

In the completely ballistic limit (contact size $a \ll l_{mfp}$), the constriction resistance derived from continuum heat transfer theory (R_{cs}), is no longer valid (diffusive theory is strictly valid when $a \gg l_{mfp}$). Assessing the rate of phonons passing through a small constriction by treating phonons as quasi-ballistic particles [57] and assuming a frequency-independent group velocity v_g (gray medium approximation [58]) that is calculated based on realistic dispersion relations [31], Prasher [56] showed that the net heat flux from material 1 to material 2 through the constriction in the ballistic limit can be expressed as

$$q'' = \frac{U_1(T_1) \cdot v_{g \cdot 1} - U_2(T_2) \cdot v_{g \cdot 2}}{4}, \qquad (31)$$

where U is the energy per unit volume of lattice vibrations under the Debye approximation. According to the definition of volumetric lattice (i.e., phonon) specific heat, Eq. (31) becomes

$$q'' = \frac{C_{l \cdot 1} \cdot T_1 \cdot v_{g \cdot 1} - C_{l \cdot 2} \cdot T_2 \cdot v_{g \cdot 2}}{4}. \qquad (32)$$

However, phonons are not classical particles, and the lattices of two materials can be different and/or loosely bonded (e.g., van der Waals bonding) so that only a fraction of the phonon energy can be transmitted through the interface. Hence, an average transmissivity Γ needs to be considered along with the phonon energy from each side such that the heat flux (Eq. (32)) should be computed as

$$q'' = \frac{\Gamma_{1 \to 2} \cdot C_{l \cdot 1} \cdot T_1 \cdot v_{g \cdot 1} - \Gamma_{2 \to 1} \cdot C_{l \cdot 2} \cdot T_2 \cdot v_{g \cdot 2}}{4}, \qquad (33)$$

Where $\Gamma_{1 \to 2}$ is the averaged transmissivity from side 1 to side 2, and $\Gamma_{2 \to 1}$ is similarly defined for the reverse direction. Assuming diffuse phonon scattering at the interface, i.e. the diffuse mismatch model of Swartz and Pohl [59], $\Gamma_{1 \to 2} = 1 - \Gamma_{2 \to 1}$. Based on the definition of total phonon intensity and Debye specific heat, Chen [31] proposed a relatively simple expression for the average transmissivity between dissimilar materials,

$$\Gamma_{1 \to 2} = \frac{C_{l \cdot 2} \cdot v_{g \cdot 2}}{C_{l \cdot 1} \cdot v_{g \cdot 1} + C_{l \cdot 2} \cdot v_{g \cdot 2}}. \qquad (34)$$

If the contacting materials are the same, then $\Gamma_{1 \to 2} = 1$. Adopting Chen's relation for the average transmissivity (Eq. (34)), the definition of surface heat flux becomes

$$q'' = \frac{1}{4} \frac{C_{l \cdot 1} \cdot v_{g \cdot 1} \cdot C_{l \cdot 2} \cdot v_{g \cdot 2}}{C_{l \cdot 1} \cdot v_{g \cdot 1} + C_{l \cdot 2} \cdot v_{g \cdot 2}}(T_1 - T_2), \qquad (35)$$

and the area-normalized ballistic resistance R''_b at individual CNT contacts can be expressed as

$$R''_b = \frac{T_1 - T_2}{q''} = \frac{4(C_{l \cdot 1} \cdot v_{g \cdot 1} + C_{l \cdot 2} \cdot v_{g \cdot 2})}{C_{l \cdot 1} \cdot v_{g \cdot 1} \cdot C_{l \cdot 2} \cdot v_{g \cdot 2}}. \qquad (36)$$

Note that R''_b is independent of the contact size a while, in contrast, R''_{cs} is proportional to a as shown in the foregoing development. Because Eq. (36) is formulated for isotropic solids, the anisotropy of CNTs is considered here by using single representative phonon group velocities that depend on CNT contact geometry as discussed below. The derivation of Eq. (36) is based on transport across interfaces in intimate contact. In a recent study involving molecular dynamics simulations [34], increased interface spacing, i.e., a departure from truly intimate contact, was shown to significantly increase R''_b. Consequently, R''_b serves as a lower bound on the thermal resistance at the van der Waals bonded CNT contacts. Eq. (36) does not explicitly account for additional thermal resistance in the ballistic transport regime that could occur because of mismatches in the phonon densities of states of a CNT and a bulk substrate [35]. This resistance is most prevalent when the dominant phonon wavelength (λ_d) exceeds the CNT diameter [35,36] ($\lambda_d \approx h v_g/k_B T$, where h is the Planck constant, v_g is the velocity of phonons, k_B is the Boltzmann constant, and T is the temperature [60]). However, as recently calculated [35,36], the thermal boundary resistance due to phonon confinement in CNTs is only significant at very low temperatures (~10 K or less for multiwalled CNTs [35] and less than 55 K for single-walled CNTs [36]).

3.3.2. Magnitude of ballistic thermal resistance

As inputs, Eq. (36) requires phonon velocities (v_g) and volumetric phonon specific heats (C_l). Table 2 includes the phonon properties of Cu, Ag, Ni, Ti, and multiwalled CNTs (MWCNTs) used for the present room-temperature ballistic resistance calculations. The lattice specific heats of Cu, Ag, Ni, and Ti were estimated based on the Debye model [61]. The associated phonon group velocities were approximated as the sound velocities in the shear direction [62], and these are consistent with the phonon group velocities from the Debye model [61].

Several studies have reported values for the phonon velocities [1,2,63,64] and specific heats [65–67] of CNTs. However, at temperatures above approximately 10 K, Prasher [35] indicated that using the phonon dispersion of graphite as an approximation for MWCNTs produces accurate predictions of specific heat and thermal conductivity. Therefore, the phonon velocities and volumetric specific heat of graphite [35] are assumed for MWCNTs in this study. The elastic constant of graphite in the basal plane (36 GPa) differs from the elastic constant along the c-axis (2.26 GPa) – the

Table 2
Phonon properties of Cu, Ag, Ni, Ti, and MWCNTs at room-temperature.

Material	C_l (kJ/m³K)	v_g (m/s)
Cu	3343	2325
Ni	3468	2990
Ag	2362	1640
Ti	2190	3120
MWCNT	1582	14,800[a], 1000[b]

[a] Basal plane.
[b] Along the c-axis.

direction perpendicular to the basal plane – consequently the phonon velocities along the respective directions differ, as indicated in Table 2. Because heat is predominantly transmitted by phonons with velocities perpendicular to the plane of contact, the basal plane phonon velocity is applicable for calculating R_b'' at the CNT–growth substrate contacts, and the c-axis phonon velocity is applicable for calculating R_b'' where the side walls of free CNT ends contact each other or an opposing surface.

By analogy to electron transport across constrictions, Prasher [56] suggested that the thermal resistance at constrictions of size $a \sim l_{mfp}$ between the same materials can be calculated accurately using $R_c = R_{cs} + R_b$, where in the limits $a \gg l_{mfp}$ and $a \ll l_{mfp}$, R_c reduces to R_{cs} and R_b, respectively. This relation was also claimed to be valid for constrictions between dissimilar materials [56]. Therefore, the total area-normalized thermal resistance at an individual CNT contact can be expressed as

$$R_{c,i}'' = R_{cs,i}'' + R_b''. \tag{37}$$

where we note that the absence of a subscript i on the ballistic resistance term reflects the fact that this resistance is independent of contact size (see Eq. (36)).

Estimates of R_b'' and $R_{c,i}''$ at room temperature are calculated using Eqs. (36) and (37), and the values of $R_{cs,i}''$ calculated earlier based on conservative assumptions for the different contact arrangements that individual CNTs can assume in CNT array interfaces. These results are displayed in Table 3. For almost all contact scenarios, the constriction resistance ($R_{cs,i}''$) is much smaller than the ballistic resistance (R_b''). In fact, as shown in Table 3, R_b'' at CNT contacts can be orders of magnitude greater than $R_{cs,i}''$. Because the phonon group velocity of MWCNTs is an order of magnitude higher in the basal plane than along the c-axis (see Table 2), and Ti has a relatively low thermal conductivity, the significance of $R_{cs\cdot Ti-CNT,i}''$ in calculating $R_{c\cdot Ti-CNT,i}''$ is relatively high. The ballistic resistance R_b'' between metallic and dielectric solids in the 150–300 K temperature range has been experimentally measured to range from 1.0×10^{-2} to 5.0×10^{-2} mm² K/W [68], which is approximately an order of magnitude greater than the estimates of R_b'' given here. This discrepancy is likely caused by much lower phonon velocities in dielectrics as compared to MWCNTs. The ballistic resistance R_b'' for metal–metal interfaces was measured at room temperature to be $\sim 10^{-3}$ mm² K/W [69], which is in good agreement with the resistances calculated here for MWCNT–metal interfaces. Assuming published values [31] for the phonon specific heat and phonon group velocity of Si, Eq. (36) was used to estimate R_b'' at a Si–Cu interface at room temperature. The estimated value of 2.72×10^{-3} mm² K/W differs by only 20% from the value estimated by Reddy et al. [70] (3.33×10^{-3} mm² K/W at 350 K) based on the diffuse mismatch model and approximating the full phonon dispersion relationship over the entire Brillouin zone with the Born–von Karman lattice dynamics model.

3.4. Total contact resistance of CNT array interfaces

To assess overall interface resistance, thermal circuits can be configured for one-sided (Fig. 5a) and two-sided (Fig. 5b) CNT array interface types. The main components for the area-normalized total thermal resistance of CNT interfaces include three elements. The first is the resistance at the growth substrate (GS–CNT) interface

$$R_{GS-CNT}'' = \left[\sum_i \frac{N_i(b_{CNT,i}) \cdot \pi \cdot b_{CNT,i}^2}{R_{cs\cdot GS-CNT,i}'' + R_{b\cdot GS-CNT}''} \right]^{-1} \approx \frac{\bar{R}_{c\cdot GS-CNT}''}{\Phi}. \tag{38}$$

The second component is the diffusive resistance of the bulk CNT array(s)

$$R_{array}'' = \frac{t}{k_{eff\cdot array}}, \tag{39}$$

which has been assessed with an effective array thermal conductivity and the estimated CNT array layer thickness at a given applied pressure (Eq. (10)). The third component is the resistance at the dry, opposing substrate (CNT–OS) interface

$$R_{CNT-OS}'' = \frac{\bar{R}_{cs\cdot CNT-OS}'' + \bar{R}_{b\cdot CNT-OS}''}{n \cdot \bar{a}_{x\cdot CNT-OS} \cdot \bar{a}_{y\cdot CNT-OS}} = \frac{\bar{R}_{c\cdot CNT-OS}'' \cdot A}{A_{r\cdot free\ ends}}, \tag{40}$$

or the dry contacts between interfacing CNT arrays (CNT–CNT)

$$R_{CNT-CNT}'' = \frac{\bar{R}_{cs\cdot CNT-CNT}'' + \bar{R}_{b\cdot CNT-CNT}''}{n' \cdot \bar{a}_{x\cdot CNT-CNT} \cdot \bar{a}_{y\cdot CNT-CNT}} = \frac{\bar{R}_{c\cdot CNT-CNT}'' \cdot A}{A_{r\cdot free\ ends}'}. \tag{41}$$

The resistances $\bar{R}_c''$ in the rightmost sides of Eqs. (38), (40), and (41) represent the thermal resistances at individual CNT contacts (Eq. (37)) comprising ballistic and constriction components. These resistances are estimated using the average CNT radius $\bar{b}_{CNT}$ of a given array and the corresponding contact size $\bar{a}_x$, which is calculated using $\bar{b}_{CNT}$ and the data in Fig. 3b. The real contact areas $A_{r\cdot free\ ends}$ and $A_{r\cdot free\ ends}'$ can be determined from Eqs. (19) and (20), respectively.

The total one-sided CNT interface resistance is

$$R_{GS-CNT-OS}'' = R_{GS-CNT}'' + R_{array}'' + R_{CNT-OS}'', \tag{42}$$

and the total two-sided CNT interface resistance is

$$R_{GS-CNT-CNT-GS}'' = R_{GS\cdot 1-CNT}'' + R_{array\cdot 1}'' + R_{CNT-CNT}'' + R_{array\cdot 2}'' + R_{GS\cdot 2-CNT}''. \tag{43}$$

The derivations of Eqs. (42) and (43) are based on thermal transport across ideal interfaces in intimate contact as well as the assumption of perfect CNT anchoring to the growth substrate; therefore, estimates based on these equations should provide lower bounds for the total thermal resistance of CNT array interfaces because contact is less intimate at free CNT ends, and the degree of CNT anchoring can vary with choice of growth substrate and fabrication approach [14,24].

The thicknesses of the arrays typically used for CNT array thermal interfaces range from 10–30 μm [14], and because of their

Table 3
Estimates of thermal resistance at individual CNT contacts at room temperature. The upper limit of constriction resistance (R_{cs}'') is estimated using a CNT radius b_{CNT} of 50 nm and assuming that the constriction alleviation factor Ψ is equal to 1. The ballistic resistance (R_b'') is estimated using Eq. (36) and the phonon properties in Table 2, and R_c'' is the sum of the ballistic and constriction resistances (see Eq. (37)).

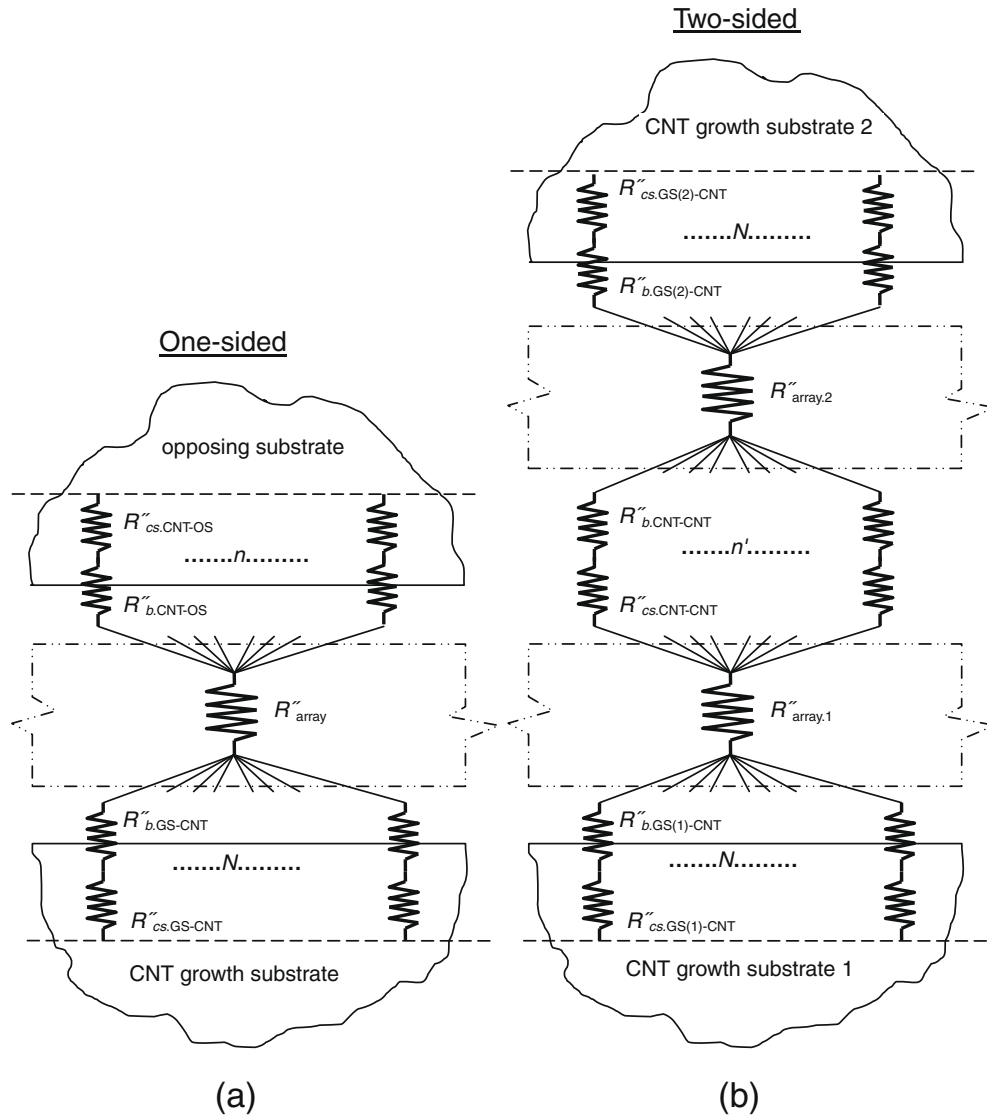| Contact type	R_{cs}''(mm²K/W)	R_b''(mm²K/W)	R_c''(mm²K/W)
Ti-CNT$_c$	1.8×10^{-3}	7.6×10^{-4}	2.6×10^{-3}
CNT–Ni	6.7×10^{-5}	2.9×10^{-3}	2.9×10^{-3}
CNT–Cu	1.7×10^{-5}	3.0×10^{-3}	3.0×10^{-3}
CNT–Ag	1.6×10^{-5}	3.6×10^{-3}	3.6×10^{-3}
CNT–CNT	4.5×10^{-6}	2.5×10^{-3}	2.5×10^{-3}

$_c$, at CNT roots.

Fig. 5. Thermal resistance networks for CNT array interfaces. (a) One-sided CNT array interface. (b) Two-sided CNT array interface.

high intrinsic thermal conductivity, the diffusive resistance (R''_{array}) of the array(s) is usually less than 10% of the measured total resistance for both one- and two-sided interfaces. For example, with an effective thermal conductivity of approximately 80 W/mK [15] and an array thickness of 5 μm after compression, R''_{array} would be approximately 6.3×10^{-2} mm^2 K/W, whereas the overall resistance is of order 1 mm^2 K/W or larger. Therefore, on average, variations of the effective thermal conductivity and CNT layer thickness are not critical in the overall resistance estimation, which is dominated by the local interfaces within the overall structure.

With $N \geqslant n$ or n' (by definition) and $\bar{b}_{\text{CNT}} \gg \bar{a}_{x \cdot \text{CNT}-\text{OS}}$ or $\bar{a}_{x \cdot \text{CNT}-\text{CNT}}$, the contact area at the free CNT ends interfaces (CNT–OS and CNT–CNT) is much less than the contact area at the growth substrate interfaces (GS–CNT), i.e. $A_{r \cdot \text{free ends}}/A$ or $A'_{r \cdot \text{free ends}}/A \ll \Phi$. For example, at $P = 10^4$ kPa $A_{r \cdot \text{free ends}}/A$ is 6.3×10^{-3} and Φ is 2.5×10^{-1} for the CNT array interface in Fig. 4. Therefore, because the total thermal resistances at individual CNT contacts ($R''_{c \cdot \text{GS}-\text{CNT}}, R''_{c \cdot \text{CNT}-\text{OS}}$, and $R''_{c \cdot \text{CNT}-\text{CNT}}$) have the same order of magnitude ($\sim 10^{-3}$ mm^2 K/W – see Table 3), the total thermal contact resistance of one-sided (Eq. (42)) or two-sided (Eq. (43)) CNT array interfaces is predominantly determined by the total contact area achieved and the total thermal resistance at the interface to the free CNT ends. Furthermore, because of the very small sizes of the van der Waals-bonded individual CNT contacts, the total thermal resistance at the free CNT ends interface is dominated by the ballistic thermal resistance instead of the constriction resistance.

Because of the relatively small contribution of the bulk CNT array's diffusive resistance and the negligible effect of k_{CNT} via R''_{cs} in determining the resistance at individual CNT contacts, the present model suggests that the high inherent thermal conductivity of CNTs is not explicitly the main factor that produces good thermal interface performance. However, the phonon group velocity and specific heat of CNTs significantly affect the ballistic thermal resistance R''_b.

3.4.1. Effects of contact pressure, volume ratio, and conformability

According to the foregoing development, the pressure dependence of the thermal resistance of CNT array interfaces is primarily determined by the change in contact area at the free CNT ends (Eq. (19) or Eq. (20)). Consequently, the ratio of real to nominal contact area achieved at the free CNT ends scales as

$$\frac{A'_{r \cdot \text{free ends}}}{A} \left(\text{or } \frac{A'_{r \cdot \text{free ends}}}{A} \right) \propto \frac{1}{1 + c_2 \cdot P^{-1}}, \tag{44}$$

where $c_2 = \sigma_R \cdot \Phi \cdot (\bar{a}_x / \bar{b}_{CNT})$. Therefore, considering Eq. (42) or (43) in combination with Eq. (44), the total thermal contact resistance of CNT array interfaces (one- or two-sided) scales with pressure as

$$R'' \propto 1 + c_2 \cdot P^{-1}. \qquad (45)$$

With the pressure dependence of Eqs. (44) and (45), contact area and total thermal resistance become constant when $P \gg c_2$. The present model assumes that the CNT array heights are uniform and larger than the average peak-to-valley height (R_z) of surface asperities on the contacting substrates (growth or opposing). Consequently, any effects of surface roughness on the pressure dependence of contact area and thermal resistance are not included in this model. Given the relatively tall array heights (10–30 μm) that are typically utilized in CNT array thermal interfaces [12–24], neglecting surface roughness effects is a reasonable assumption because the CNTs can bridge the gaps formed by substrates with common surfaces finishes.

Considering the foregoing analysis, the thermal resistance of CNT array interfaces as a function of applied pressure essentially depends on the amount of real contact area achieved at the free CNT ends interface as a function of pressure. Therefore, identical to the contact area dependencies, the pressure-dependent thermal resistance of a CNT array interface primarily depends on Φ and array conformability, which is quantified by the array's resistance to mechanical compression, $\sigma_R = c_1 \cdot E_b \cdot \Phi^3$. Decreased σ_R and increased Φ decreases thermal resistance at the CNT array interface; however, as evidenced by the functional dependence of σ_R on Φ, an optimal combination of these parameters that achieves low thermal resistance must be established.

3.4.2. Application of the model to experimental results

The ballistic resistance R''_b essentially assumes perfect contact between a CNT and its underlying substrate (or another CNT in the case of a two-sided interface), and this idealization can cause a significant underprediction of thermal resistance. This issue is particularly acute at van der Waals bonded CNT contacts such as those between opposing CNTs and those between the free tips of CNTs and a bulk surface. For example, application of the foregoing theory (see Eqs. (19)–(43)) to a one-sided interface produces predictions of total interface resistances of the order of 1 mm² K/W or less, which is much smaller than experimental observations as discussed below. Furthermore, refined experiments that enable extraction of *local* resistances within the interface [20] have revealed that the dominant series resistance occurs at the free tips of the CNT array.

To account for such non-ideal interfaces, the resistance at individual CNT contacts $\bar{R}''_{c \cdot CNT-OS}$ (or $\bar{R}''_{c \cdot CNT-CNT}$ for two-sided interfaces) in Eqs. (40)–(43), which is approximately equal to the ballistic resistance $R''_{b \cdot CNT-OS}$ (or $R''_{b \cdot CNT-CNT}$) (see Eq. (37), Table 3, and the above discussions), is replaced with a resistance $R''_{vdW \cdot CNT-OS}$ (or $R''_{vdW \cdot CNT-CNT}$) that nominally represents the effective resistance at the van der Waals interface between the free CNT tips and the opposing surface. Further, because the diffusive resistance of the compressed CNT array(s) and the resistance at the growth substrate interface are not critical in the overall resistance estimation, Eq. (42) is simplified as follows for a one-sided interface

$$R''_{GS-CNT-OS} \approx \frac{R''_{vdW \cdot CNT-OS} \cdot A}{A_{r \cdot free\ ends}}, \qquad (46)$$

where $R''_{vdW \cdot CNT-OS}$ is an effective resistance that is estimated from experiments [14,17,23]. For two-sided configurations, the measured thermal resistances at the interfaces to the growth substrates were observed to be comparable to the resistance at the mating CNT–CNT interface [20]. Therefore, Eq. (43) is simplified to model the measured thermal resistances of a two-sided CNT array interface [20] as

$$R''_{GS-CNT-CNT-GS} \approx (R''_{GS \cdot 1-CNT} + R''_{GS \cdot 2-CNT}) + \frac{R''_{vdW \cdot CNT-CNT} \cdot A}{A'_{r \cdot free\ ends}}, \qquad (47)$$

where $R''_{vdW \cdot CNT-CNT}$ again serves as a parameter estimated from experiments, and the measured values of $R''_{GS \cdot 1-CNT}$ and $R''_{GS \cdot 2-CNT}$ [20] were used. Significantly, for both one- and two-sided interfaces, the foregoing approach of estimating an effective ballistic resistance for a given unit of true contact area – R''_{vdW} – retains the essential character of the model in that this resistance is not expected to depend on pressure (the primary variable of experimental variation considered here). Rather, the pressure variation is captured in the ratio of nominal area to true contact area in Eqs. (46) and (47).

Because load–displacement data are not available explicitly, the parameters c_1 and t' in Eqs. (19) and (20) – the expressions for contact area – also served as fitting parameters in the one- and two-sided CNT array interface models Eqs. (46) and (47). The mean array thickness (t_m) is assumed for t_o. A least-squares routine was used to fit Eqs. (46) and (47) to the measured thermal contact resistance data [14,17,20,23], and Fig. 6 illustrates the close agreement between the model and experimental data.

The regression parameters c_1 and t' are presented in Table 4. Because c_1 is a fitting parameter that accounts for variations in array characteristics, the fitted values of c_1 can span a wide range of values as shown in Table 4. The R''_{vdW} estimates are shown in Table 5 along with R''_b for comparison. Notably, R''_b is less than R''_{vdW} by one to two orders of magnitude. However, in recent molecular dynamics simulations of heat transport across a van der Waals-bonded interface between two single-walled CNTs in contact, thermal resistance was calculated to be approximately 0.1 mm²·K/W at an atomic separation distance of 0.4 nm [34]; this value is in close agreement with the values of R''_{vdW} in the present study.

Fig. 6 illustrates that the pressure scaling of thermal contact resistance for CNT array interfaces given by Eq. (45) predicts experimentally observed pressure trends with good agreement. For the pressure range shown in Fig. 6, the thermal contact resistance of the Si/Ti–CNT–CNT–Ti/Cu interface (*i.e.,* a two-sided CNT array) [20] is approximately constant, indicating that $P \gg c_2$ for this data. Pressure saturation of thermal contact resistance occurs under larger applied pressures for the other (one-sided) CNT array interface data shown in Fig. 6. The effects of the parameters σ_R and Φ on the magnitude of total thermal resistance of the CNT array interfaces
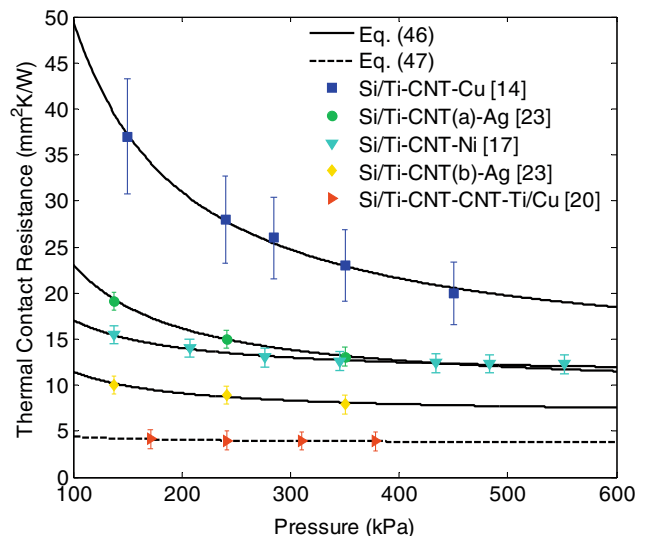

Fig. 6. Eq. (46) or Eq. (47) fit to thermal contact resistance data [14,17,20,23] as a function of applied pressure. The fitting parameters were t', c_1, and R''_{vdW}.

Table 4
Characteristics of various CNT arrays used as thermal interface materials. The parameters t' and c_1 are obtained from fitting Eqs. (46) or (47) to experimental thermal contact resistance data [14,17,20,23].

Interface	Φ	$\bar{b}_{CNT}$ (nm)	t_m (μm)	t' (μm)	c_1	σ_R (MPa)
Si/Ti–CNT–Cu [14]	0.24	16	13	2.5	0.011	15.06
Si/Ti–CNT–Ni [17]	0.10	50	30	1.5	0.08	8.01
Si/Ti-CNT(a)–Ag [23]	0.35	4	20	5.5	0.0008	3.22
Si/Ti-CNT(b)–Ag [23]	0.45	20	20	4.5	0.0002	1.73
Si/Ti–CNT–CNT–Ti/Cu [20]	0.40[d]	15[d]	35[d]	5.2[d]	0.0002[d]	1.19[d]

[d] Effective properties of both arrays.

Table 5
Thermal resistance at the interface of an individual CNT contacting an opposing substrate or an opposing CNT. R''_{vdW} is determined from fitting Eq. (46) or (47) to experimental thermal contact resistance data [14,17,20,23], and R''_b (determined from Eq. (36)) is reproduced from Table 3 for comparison.

Interface to individual free CNT end	R''_b (mm^{2}K/W)	R''_{vdW} (mm^{2}K/W)
CNT–Cu [14]	0.0030	~0.1
CNT–Ni [17]	0.0029	~0.05
CNT(a)–Ag [23]	0.0036	~0.2
CNT(b)–Ag [23]	0.0036	~0.1
CNT–CNT [20]	0.0025	~0.07

presented here can be qualitatively understood by comparing the data in Table 4 to the results in Fig. 6. Overall, interfaces with smaller values of σ_R exhibit lower thermal contact resistances. It is difficult to infer a trend directly related to Φ considering the present data, however its effects are accounted for in σ_R, and t' or the expression $(t_m - t')/[(\sqrt[3]{2} - 1) \cdot t' + t_m]$, which can be viewed as an additional compressibility metric that ranges from approximately 0.7 to 0.9 for the arrays here.

Using the parameters obtained by fitting compression data (Table 1) and assuming $k_{eff,array} = 80$ W/mK [16], Eq. (42), which assumes intimate and ideal contact at free CNT ends, was used to estimate the lower bounds of total thermal resistance for the Cu/Ti–CNT–Cu interface in Ref. [39]. As illustrated in Fig. 7, the thermal resistances predicted by Eq. (42) are at least an order of magnitude less than the model predictions based on Eq. (46) (using the fitted value of R''_{vdW} for a CNT–Cu contact − 0.1 mm^2 K/W). This result is consistent with the fact that thermal resistance at chemically bonded interfaces in good contact can be orders of
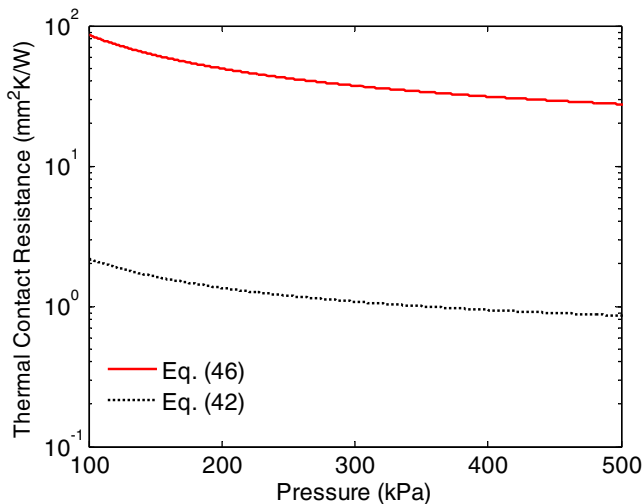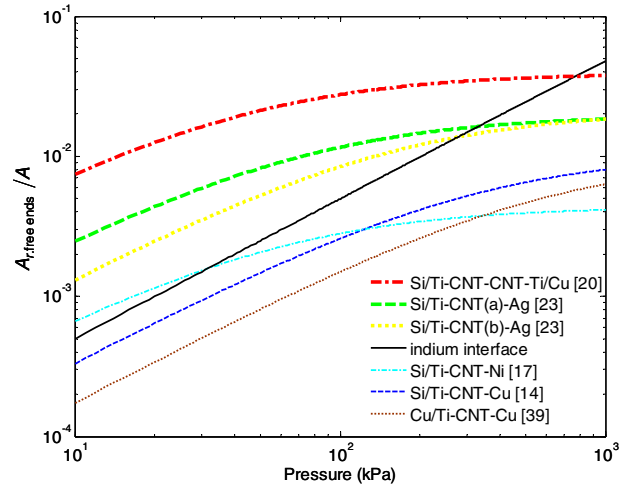
Fig. 8. Ratio of real to nominal contact area at interface to free CNT ends. The parameters in Tables 1 and 4, and Eq. (19) or Eq. (20) were used for the contact area estimations. An area ratio prediction based on traditional theory [42] for a contacted indium surface is shown for comparison.

magnitude less than the thermal resistance at interfaces with larger atomic separation and accordingly weaker bonds [34].

Utilizing the parameters in Tables 1 and 4, Eqs. (19) and (20) were used to predict the real contact area achieved as a function of pressure at free-CNT-end interfaces in different CNT array interface assemblies. As shown in Fig. 8, the contact area established by the dense, substrate-supported CNT arrays compares favorably to the area achieved in a soft indium [71] interface. Consequently, the combination of indium-like mechanical compliance and large thermal conductances – among many other notably characteristics [1] – makes CNT arrays an attractive thermo-mechanical material that may find broad use.

A CNT array interface with an optimal combination of small values of σ_R and large values of Φ will achieve the lowest thermal contact resistance. For example, the Si/Ti–CNT(b)–Ag interface [23] in Fig. 6 achieves the lowest one-sided thermal resistances, and the two-sided Si/Ti–CNT–CNT–Ti/Cu interface [20] in Fig. 6 achieves the lowest overall resistance. As a result of this analysis, σ_R and Φ are proposed as explicit metrics for optimizing CNT array properties for improved thermal contact conductance.

4. Summary and conclusions

A contact resistance model has been developed in this work to describe heat transfer across CNT array interfaces. Detailed constriction and ballistic resistance analysis at individual CNT growth-substrate contacts or free-end contacts (to an opposing substrate or CNT array) were presented. The effects of CNT array properties such as diameter, density, and distribution have been explicitly incorporated in the model. The model predictions – using

Fig. 7. Lower bounds on thermal resistance for the one-sided Cu/Ti–CNT–Cu interface in Ref. [39] predicted using Eq. (42). A prediction based on Eq. (46) (assuming the fitted value of R''_{vdW} for CNT–Cu contacts) is shown for comparison.

an adjustable factor (c_1), the incompressible thickness of the CNT array (t'), and the thermal resistance at van der Waals bonded, individual free-CNT-end contacts R''_{vdW} as fitting parameters – are in close agreement with measured thermal contact resistance data and accurately reproduce experimental pressure trends. The fitting results indicate that R''_{vdW} is underpredicted by one to two orders of magnitude by a ballistic resistance analysis presented here that assumes ideal, chemically bonded interfaces. However, the regressed R''_{vdW} values are on the same order as results from molecular dynamics simulations that consider larger atomic separations at the CNT contacts.

The CNT array contact resistance model reveals that the thermal resistances at single-CNT contacts dominate the thermal transport across CNT array interfaces such that the effective thermal conductivity of the CNT array has little effect on interface resistance for moderate array heights (< 30 μm). The model also reveals that the overall performance of CNT array interfaces is predominately determined by the ballistic thermal resistance – instead of constriction resistance – at free-CNT-end contacts to an opposing substrate surface or CNT array, and that the total thermal resistance of CNT array interfaces can be reduced by optimizing the array conformability and density such that the true contact area established in the interface is maximized.

References

[1] M.S. Dresselhaus, G. Dresselhaus, A. Jorio, Unusual properties and structure of carbon nanotubes, Ann. Rev. Mater. Res. 34 (2004) 247–278.
[2] M.S. Dresselhaus, P.C. Eklund, Phonons in carbon nanotubes, Adv. Phys. 49 (2000) 705–814.
[3] J.W. Che, T. Cagin, W.A. Goddard, Thermal conductivity of carbon nanotubes, Nanotechnology 11 (2000) 65–69.
[4] S. Berber, Y.K. Kwon, D. Tomanek, Unusually high thermal conductivity of carbon nanotubes, Phys. Rev. Lett. 84 (2000) 4613–4617.
[5] M.A. Osman, D. Srivastava, Temperature dependence of the thermal conductivity of single-wall carbon nanotubes, Nanotechnology 12 (2001) 21–24.
[6] S. Maruyama, A molecular dynamics simulation of heat conduction of a finite length single-walled carbon nanotube, Microscale Thermophys. Eng. 7 (2003) 41–50.
[7] J. Hone, M. Whitney, C. Piskoti, A. Zettl, Thermal conductivity of single-walled carbon nanotubes, Phys. Rev. B 59 (1999) 2514–2516.
[8] P. Kim, L. Shi, A. Majumdar, P.L. McEuen, Thermal transport measurements of individual multiwalled nanotubes, Phys. Rev. Lett. 87 (2001) 215502.
[9] A. Cao, P.L. Dickrell, W.G. Sawyer, M.N. Ghasemi-Nejhad, P.M. Ajayan, Super-compressible foamlike carbon nanotube films, Science 310 (2005) 1307–1310.
[10] C.P. Deck, J. Flowers, G.S.B. McKee, K. Vecchio, Mechanical behavior of ultralong multiwalled carbon nanotube mats, J. Appl. Phys. 101 (2007) 023512.
[11] J. Suhr, P. Victor, L. Ci, S. Sreekala, X. Zhang, O. Nalamasu, P.M. Ajayan, Fatigue resistance of aligned carbon nanotube arrays under cyclic compression, Nat. Nanotechnol. 2 (2007) 417–421.
[12] H.F. Chuang, S.M. Cooper, M. Meyyappan, B.A. Cruden, Improvement of thermal contact resistance by carbon nanotubes and nanofibers, J. Nanosci. Nanotechnol. 4 (2004) 964–967.
[13] Q. Ngo, B.A. Cruden, A.M. Cassell, G. Sims, M. Meyyappan, J. Li, C.Y. Yang, Thermal interface properties of Cu-filled, vertically aligned carbon nanofiber arrays, Nano Lett. 4 (2004) 2403–2407.
[14] J. Xu, T.S. Fisher, Enhanced thermal contact conductance using carbon nanotube array interfaces, IEEE Trans. Compon. Packag. Technol. 29 (2006) 261–267.
[15] X.J. Hu, A.A. Padilla, J. Xu, T.S. Fisher, K.E. Goodson, 3-omega measurements of vertically oriented carbon nanotubes on silicon, ASME J. Heat Transfer 128 (2006) 1109–1113.
[16] X. Wang, Z. Zhong, J. Xu, Noncontact thermal characterization of multiwall carbon nanotubes, J. Appl. Phys. 97 (2005) 064302.
[17] Y. Xu, Y. Zhang, E. Suhir, X. Wang, Thermal properties of carbon nanotube array used for integrated circuit cooling, J. Appl. Phys. 100 (2006) 074302.
[18] J. Xu, T.S. Fisher, Enhancement of thermal interface materials with carbon nanotube arrays, Int. J. Heat Mass Transfer 49 (2006) 1658–1666.
[19] B.A. Cola, X. Xu, T.S. Fisher, Increased real contact in thermal interfaces: a carbon nanotube/foil material, Appl. Phys. Lett. 90 (2007) 093513.
[20] B.A. Cola, J. Xu, C. Cheng, X. Xu, H. Hu, T.S. Fisher, Photoacoustic characterization of carbon nanotube array thermal interfaces, J. Appl. Phys. 101 (2007) 054313.
[21] T. Tong, Y. Zhao, L. Delzeit, A. Kashani, M. Meyyappan, A. Majumdar, Dense vertically aligned multiwalled carbon nanotube arrays as thermal interface materials, IEEE Trans. Compon. Packag. Technol. 30 (2007) 92–99.
[22] P.B. Amama, B.A. Cola, T.D. Sands, X. Xu, T.S. Fisher, Dendrimer-assisted controlled growth of carbon nanotubes for enhanced thermal interface conductance, Nanotechnology 18 (2007) 385303.
[23] B.A. Cola, P.B. Amama, X. Xu, T.S. Fisher, Effects of growth temperature on carbon nanotube array thermal interfaces, ASME J. Heat Transfer 130 (2008) 114503.
[24] B.A. Cola, M.A. Capano, P.B. Amama, X. Xu, T.S. Fisher, Carbon nanotube array thermal interfaces for high-temperature silicon carbide devices, J. Nanoscale Microscale Thermophys. Eng. 12 (2008) 228–237.
[25] M.A. Panzer, G. Zhang, D. Mann, X. Hu, E. Pop, H. Dai, K.E. Goodson, Thermal properties of metal-coated vertically aligned single-wall carbon nanotube arrays, ASME J. Heat Transfer 130 (2008) 052401.
[26] K. Zhang, Y. Chai, F.M.M. Yuen, D.G.W. Xiao, P.C.H. Chan, Carbon nanotube thermal interface material for high-brightness light-emitting-diode cooling, Nanotechnology 19 (2008) 215706.
[27] J. Xu, Carbon nanotube array thermal interfaces, Ph.D. dissertation, Purdue University, West Lafayette, IN, 2006.
[28] S.T. Huxtable, D.G. Cahill, S. Shenogin, L. Xue, R. Ozisik, P. Barone, M. Usrey, M.S. Strano, G. Siddons, M. Shim, P. Keblinski, Interfacial heat flux in carbon nanotube suspensions, Nat. Mater. 2 (2003) 731–734.
[29] S. Shenogin, L. Xue, R. Ozisik, P. Keblinskia, D.G. Cahill, Role of thermal boundary resistance on the heat flow in carbon-nanotube composites, Appl. Phys. Lett. 87 (2005) 211908.
[30] S. Maruyama, in: W.J. Minkowycz, E.M. Sparrow, J.Y. Murthy (Eds.), Handbook of Numerical Heat Transfer, second ed., Wiley, New York, 2006, pp. 659–696 (Chapter 21).
[31] G. Chen, Thermal conductivity and ballistic-phonon transport in the cross-plane direction of superlattices, Phys. Rev. B 57 (1998) 14958–14973.
[32] G. Wexler, The size effect and the non-local Boltzmann transport equation in orifice and disk geometry, Proc. Phys. Soc. 89 (1966) 927–941.
[33] L. Weber, E. Gmelin, H.J. Queisser, Thermal resistance of silicon point contacts, Phys. Rev. B 40 (1989) 1244–1249.
[34] H. Zhong, J. Lukes, Interfacial thermal resistance between carbon nanotubes: molecular dynamics simulations and analytical thermal modeling, Phys. Rev. B 74 (2006) 125403.
[35] R. Prasher, Thermal boundary resistance and thermal conductivity of multiwalled carbon nanotubes, Phys. Rev. B 77 (2008) 075424.
[36] R. Prasher, T. Tong, A. Majumdar, An acoustic and dimensional mismatch model for thermal boundary conductance between a vertical mesoscopic nanowires/nanotube and a bulk substrate, J. Appl. Phys. 101 (2007) 104312.
[37] C.M. van Wyk, Note on the compressibility of wool, J. Textile Inst. 37 (1946) T285–T292.
[38] S. De Jong, J.W. Snaith, N.A. Michie, A mechanical model for the lateral compression of woven fabrics, Textile Res. J. 56 (1986) 759–767.
[39] M. Park, B.A. Cola, T. Siegmund, J. Xu, M.R. Maschmann, T.S. Fisher, H. Kim, Effects of a carbon nanotube layer on electrical contact resistance between copper substrates, Nanotechnology 17 (2006) 2294–2303.
[40] Y. Zhang, E. Suhir, Y. Xu, Effective young's modulus of carbon nanofiber array, J. Mater. Res. 21 (2006) 2948–2954.
[41] T. Tong, Y. Zhao, L. Delzeit, A. Kashani, M. Meyyappan, A. Majumdar, Height independent compressive modulus of vertically aligned carbon nanotube arrays, Nano Lett. 8 (2008) 511–515.
[42] C.V. Madhusudana, Thermal Contact Conductance, Springer-Verlag, New York, 1996.
[43] M.R. Maschmann, P.B. Amama, A. Goyal, Z. Iqbal, R. Gat, T.S. Fisher, Parametric study of synthesis conditions in plasma-enhanced CVD of high-quality single-walled carbon nanotubes, Carbon 44 (2006) 10–18.
[44] V. Bahadur, J. Xu, Y. Liu, T.S. Fisher, Thermal resistance of nanowire–plane interfaces, ASME J. Heat Transfer 127 (2005) 664–668.
[45] S. Akita, H. Nishijima, Y. Nakayama, Influence of stiffness of carbon-nanotube probes in atomic force microscopy, J. Phys. D 33 (2000) 2673–2677.
[46] I. Palaci, S. Fedrigo, H. Brune, C. Klinke, M. Chen, E. Riedo, Radial elasticity of multiwalled carbon nanotubes, Phys. Rev. Lett. 94 (2005) 175502.
[47] B.T. Kelly, Physics of Graphite, Applied Science, London, 1981.
[48] J. Gaillard, M. Skove, A.M. Rao, Mechanical properties of chemical vapor deposition-grown multiwalled carbon nanotubes, Appl. Phys. Lett. 86 (2005) 233109.
[49] K. Enomoto, S. Kitakata, T. Yasuhara, N. Ohtake, T. Kuzumaki, Y. Mitsuda, Measurement of Young's modulus of carbon nanotubes by nanoprobe manipulation in a transmission electron microscope, Appl. Phys. Lett. 88 (2006) 153115.

[50] B.B. Mikic, Thermal contact conductance; theoretical considerations, Int. J. Heat Mass Transfer 17 (1974) 205–214.
[51] O. Yaglioglu, A.J. Hart, R. Martens, H. Slocum, Method of characterizing electrical contact properties of carbon nanotube coated surfaces, Rev. Sci. Instrum. 77 (2006) 095105.
[52] M. Bahrami, J.R. Culham, M.M. Yovanovich, Modeling thermal contact resistance: a scale analysis approach, ASME J. Heat Transfer 126 (2004) 896–905.
[53] M.M. Yovanovich, G.E. Schneider, Thermal constriction resistance due to a circular annular contact, Prog. Astronaut. Aeronaut. Thermophys. Spacecraft Outer Planet Entry Probes 56 (1976) 141–154.
[54] F.P. Incropera, D.P. DeWitt, Fundamentals of Heat and Mass Transfer, fifth ed., Wiley, New York, 2002.
[55] G.R. McGee, M.H. Schankula, M.M. Yovanovich, Thermal resistance of cylinder–flat contacts: theoretical analysis and experimental verification of a line-contact model, Nucl. Eng. Design 86 (1985) 369–381.
[56] R. Prasher, Predicting the thermal resistance of nanosized constrictions, Nano Lett. 5 (2005) 2155–2159.
[57] R.D. Present, Kinetic Theory of Gases, McGrew-Hill, New York, 1958.
[58] G. Chen, Size and interface effects on thermal conductivity of superlattices and periodic thin-film structures, ASME J. Heat Transfer 119 (1997) 220–229.
[59] E.T. Swartz, R.O. Pohl, Thermal boundary resistance, Rev. Modern Phys. 61 (1989) 605–668.
[60] K. Schwab, E.A. Henriksen, J.M. Worlock, M.L. Roukes, Measurement of the quantum of thermal conductance, Nature 404 (2000) 974–976.
[61] N.W. Ashcroft, N.D. Mermin, Solid State Physics, Brooks Cole, New York, 1976.
[62] R.E. Bolz, G.L. Turve, CRC Handbook of Tables for Applied Engineering Science, second ed., CRC Press, Cleveland, 1973.
[63] J.C. Lasjaunias, K. Biljakovic, P. Monceau, J.L. Sauvajo, Low-energy vibrational excitations in carbon nanotubes studied by heat capacity, Nanotechnology 14 (2003) 998–1003.
[64] R. Saito, T. Takeya, T. Kimura, G. Dresselhaus, M.S. Dresselhaus, Raman intensity of single-wall carbon nanotubes, Phys. Rev. B 57 (1998) 4145–4153.
[65] W. Yi, L. Lu, D. Zhang, Z.W. Pan, S.S. Xie, Linear specific heat of carbon nanotubes, Phys. Rev. B 59 (1999) R9015–R9018.
[66] J. Hone, M.C. Llaguno, M.J. Biercuk, A.T. Johnson1, B. Batlogg, Z. Benes, J.E. Fischer, Thermal properties of carbon nanotubes and nanotube-based materials, Appl. Phys. A 74 (2002) 339–343.
[67] C. Masarapu, L.L. Henry, B. Wei, Specific heat of aligned multiwalled carbon nanotubes, Nanotechnology 16 (2005) 1490–1494.
[68] D.G. Cahill, W.K. Ford, K.E. Goodson, G.D. Mahan, A. Majumdar, H.J. Maris, R. Merlin, S.R. Phillpot, Nanoscale thermal transport, J. Appl. Phys. 93 (2003) 793–818.
[69] B.M. Clemens, G.L. Eesley, C.A. Paddock, Time-resolved thermal transport in compositionally modulated metal films, Phys. Rev. B 37 (1988) 1085–1096.
[70] P. Reddy, K. Castelino, A. Majumdar, Diffuse mismatch model of thermal boundary conductance using exact phonon dispersion, Appl. Phys. Lett. 87 (2005) 211908.
[71] X. Cai, X. Yang, P. Zhou, Dependence of vickers microhardness on applied load in indium, J. Mater. Sci. Lett. 16 (1997) 741–742.